

# Journal of Materials Chemistry A

Accepted Manuscript



This is an *Accepted Manuscript*, which has been through the Royal Society of Chemistry peer review process and has been accepted for publication.

*Accepted Manuscripts* are published online shortly after acceptance, before technical editing, formatting and proof reading. Using this free service, authors can make their results available to the community, in citable form, before we publish the edited article. We will replace this *Accepted Manuscript* with the edited and formatted *Advance Article* as soon as it is available.

You can find more information about *Accepted Manuscripts* in the [Information for Authors](#).

Please note that technical editing may introduce minor changes to the text and/or graphics, which may alter content. The journal's standard [Terms & Conditions](#) and the [Ethical guidelines](#) still apply. In no event shall the Royal Society of Chemistry be held responsible for any errors or omissions in this *Accepted Manuscript* or any consequences arising from the use of any information it contains.



Journal Name

ARTICLE

## Facile synthesis of metal-organic framework-derived Mn<sub>2</sub>O<sub>3</sub> nanowires coated three-dimensional graphene network for high-performance free-standing supercapacitor electrodes

Dong Ji<sup>a</sup>, Hu Zhou<sup>\*b</sup>, Jian Zhang<sup>a</sup>, Yuanyuan Dan<sup>a</sup>, Hongxun Yang<sup>a</sup>, Aihua Yuan<sup>\*a</sup>

Received 00th February 2016,  
Accepted 00th February 2016

DOI: 10.1039/x0xx00000x

www.rsc.org/

This study presents a facile strategy to construct three-dimensional graphene network (3DGN) and metal-organic framework (MOF)-derived metal oxide composites as a free-standing electrode for supercapacitors for the first time. The Mn-based MOF is firstly grown *in situ* on the 3DGN substrate through a simple solution immersion method, and then the high-temperature treatment has resulted in the formation of 3DGN decorated by Mn<sub>2</sub>O<sub>3</sub> with a nanowire stacking flower-like morphology. The structure and morphology of as-prepared samples are investigated by powder X-ray diffraction, Raman spectroscopy, X-ray photoelectron spectroscopy analysis, scanning electron microscopy, element mapping, and transmission electron microscopy. The designed 3DGN/Mn<sub>2</sub>O<sub>3</sub> electrode material exhibits a high specific capacitance of 471.1 F g<sup>-1</sup> (0.21 F cm<sup>-2</sup>) at 0.2 A g<sup>-1</sup>, good rate capability of 57.3% at 5 A g<sup>-1</sup> relative to the initial value at 0.2 A g<sup>-1</sup>, and excellent long-cycle stability without decaying after 1800 charge-discharge cycles. The remarkable electrochemical performances are originated from the synergistic effect of the high electrical conductivity and large surface area of 3DGN along with the superior pseudocapacitance activity of Mn<sub>2</sub>O<sub>3</sub> nanowires. This result suggests that the 3DGN/MOF-derived metal oxide composites are promising and efficient binder-free electrode materials for high-performance supercapacitors.

### 1. Introduction

With the increasing concern regarding energy suppliers and environment pollution, there has been an urgent demand for the development of sustainable and renewable resources.<sup>1</sup> In this context, electrochemical capacitors or supercapacitors have been considered as promising candidates for energy storage because of their high power densities, fast charge-discharge rate, long operating lifetime, and low maintenance cost.<sup>2-5</sup> Transition metal oxides such as RuO<sub>2</sub>, MnO<sub>2</sub>, Mn<sub>2</sub>O<sub>3</sub>, Co<sub>3</sub>O<sub>4</sub>, NiO, Fe<sub>2</sub>O<sub>3</sub>, and Fe<sub>3</sub>O<sub>4</sub>, which are electrochemically active materials, have attracted great attention due to their exceptional pseudocapacitive properties.<sup>6-9</sup>

Recently, metal-organic frameworks (MOFs) have been widely studied owing to their large specific surface areas, high and tunable porosities, low densities, and versatile functionalities.<sup>10</sup> MOFs with specific characteristics can be fabricated through varying the type of metal ions and organic linkers.<sup>11-16</sup> This unique feature provides unlimited possibilities for constructing different kinds of nanostructured metal oxides by using MOFs as precursors or templates via thermolysis. The obtained MOF-derived metal oxides

can be size- or shape-controlled under well-adjusted preparing conditions, which is beneficial for these electrode materials to achieve superior electrochemical performances.<sup>17-32</sup> However, pseudocapacitors constructed from metal oxides often suffered from low rate capabilities and poor stabilities because of their low inherent electrical conductivities and large volume changes during the charge/discharge process.<sup>6</sup> To deal with these issues, great efforts have been made to design and fabricate metal oxides-carbon composite electrodes involving nanostructured carbon materials (carbon nanofibers, carbon nanotubes, graphene, etc), which can act as both a conductive network to increase the electrical conductivity and a volume buffer to alleviate internal stress.<sup>33-44</sup> The recently developed three-dimensional graphene network (3DGN) with a highly conducting framework, large internal surface area, and mechanical properties has been used widely as an excellent current collector in energy storage and conversion fields.<sup>45-47</sup> Especially, the 3DGN coated with different types of nanostructured metal oxides have been employed as binder-free electrode materials for high-performance supercapacitors due to their high electrical conductivities and electrochemical activities than those of pure metal oxides.<sup>48,49</sup>

Taking into account the merits of MOF-derived metal oxides and 3DGN, it is believed that the combination of both components will probably produce excellent electrochemical performances. Unfortunately, until now there are only two examples of 3DGN/MOF-derived metal oxides. Zhang has employed recently a two-step annealing strategy to construct 3DGN/metal oxides (Fe<sub>2</sub>O<sub>3</sub>, ZnO) hybrids by using MOFs (MIL-88-Fe, ZIF-8) as the precursors of metal oxides and 3DGN as the backbone, and the

School of Environmental and Chemical Engineering, Jiangsu University of Science and Technology, Zhenjiang 212003, P. R. China. \*Email - aihua.yuan@just.edu.cn (A.H. Yuan).

School of Material Science and Engineering, Jiangsu University of Science and Technology, Zhenjiang 212003, P. R. China. \*Email - zhmiaoo119@sina.com (H. Zhou).

† Footnotes relating to the title and/or authors should appear here. Electronic Supplementary Information (ESI) available: [details of any supplementary information available should be included here]. See DOI: 10.1039/x0xx00000x

properties of photocatalysis and lithium-ion batteries for both materials were explored.<sup>50</sup> As a continuation of our developed MOF-graphene hybrids for the energy-storage application,<sup>51-55</sup> we described in this work a facile two-step process by the combination of an immersion reaction and subsequent annealing treatment to fabricate 3DGN/metal oxide composites as free-standing electrode materials. As shown in Scheme 1, the high-quality 3DGN was firstly prepared by a chemical vapor deposition technique,<sup>56</sup> and then Mn-BTC ( $\text{H}_3\text{BTC}$  = 1,3,5-benzenetricarboxylic acid) crystals were grown on 3DGN via a solution immersion method. The final  $\text{Mn}_2\text{O}_3$ -anchored 3DGN hybrid was obtained after the calcination of 3DGN/Mn-BTC precursor in air. The as-synthesized 3DGN/ $\text{Mn}_2\text{O}_3$  was used directly as the current collector without any binder and conducting agent. In this composite, the 3DGN network provided the electron superhighways for charge storage and further promoted the charge-exchanging rate of active material  $\text{Mn}_2\text{O}_3$  involving the proton and electron double injecting/expelling process. As a result, this type of electrode material represented a remarkable electrochemical performance with a large specific capacitance, high rate capability and excellent cycling stability, which can be reasonably ascribed to the synergistic effect of 3DGN and  $\text{Mn}_2\text{O}_3$  components. To the best of our knowledge, this is the first work on the fabrication of MOF-derived metal oxides coated on 3DGN as electrode materials for supercapacitors.



Scheme 1 Schematic illustration for the fabrication of 3DGN/ $\text{Mn}_2\text{O}_3$ .

## 2. Experimental details

### 2.1 Chemicals

All chemicals were purchased from Shanghai Chemical Reagent Co. Ltd (China) and used as received without further purification. Nickel foam (1.0 mm thickness) was purchased from Shenzhen Six Carbon Technology (China).

### 2.2 Synthesis of 3DGN

3DGN was prepared by using a chemical vapor deposition (CVD) method. In brief, the nickel foam was put into a quartz tube and heated to 1000 °C at a ramping rate of 30 °C  $\text{min}^{-1}$  in the flow of mixed gas of Ar (300 sccm) and  $\text{H}_2$  (10 sccm). The temperature was kept at 1000 °C for 60 min and then  $\text{CH}_4$  (60 sccm) was bubbled into the tube with a mixing gas of Ar/ $\text{H}_2$  (V/V = 100/10) for 15 min when the temperature was stable. The furnace was fast cooled down to the room temperature at a cooling rate of about 100 °C  $\text{min}^{-1}$  under an Ar/ $\text{H}_2$  flow, and the 3DGN coated on Ni foam were obtained. Raman spectrum of this sample exhibited two characteristic peaks: G band at  $\sim 1585 \text{ cm}^{-1}$  assigned to the  $\text{E}_{2g}$  phonon of C  $\text{sp}^2$  atoms and 2D band at  $\sim 2690 \text{ cm}^{-1}$  corresponding to the double resonance transitions (Fig. S1).<sup>57</sup> The intensity ratio between the 2D and G bands indicates the multilayer feature of graphene foam.<sup>58</sup> The lack of defects and absence of contacts between separated graphene sheets ensure a high conductivity of such a 3D graphene monolith.<sup>59</sup> The as-prepared 3DGN with Ni was immersed in a mixture solution of  $\text{FeCl}_3$  (1 mol  $\text{L}^{-1}$ ) and HCl (1 mol  $\text{L}^{-1}$ ) at room temperature to remove Ni metal. Finally 3DGN without Ni was heated in 69 wt%  $\text{HNO}_3$  at 80 °C for 8 hours and subjected to further use.

### 2.3 Synthesis of Mn-BTC

Mn-based MOF was synthesized by following the procedure reported elsewhere with slight modifications.<sup>60</sup> Typically,  $\text{Mn}(\text{CH}_3\text{COO})_2$  (0.25 g) and PVP (K-29, 0.5 g) were dissolved in an ethanol/water (V/V = 1/1, 10 mL) system to give solution I. 0.45 g of 1,3,5-benzenetricarboxylic acid ( $\text{H}_3\text{BTC}$ ) was also dissolved in an ethanol/water (V/V = 1/1, 10 mL) to form solution II. Solution II was poured slowly into solution I under stirring and the stirring was stopped after 30 seconds. The white precipitations appeared after the reaction mixture was left unstirred and aged for 24 h. The products were collected by centrifugation, washed with equal amount of ethanol/water mixture several times, and then dried in an oven at 60 °C. The resulting sample was referred to as Mn-BTC.

### 2.3 Synthesis of $\text{Mn}_2\text{O}_3$

$\text{Mn}_2\text{O}_3$  was prepared through the calcination of Mn-BTC in a furnace under a flow of air. The temperature was firstly raised to 450 °C at a ramping rate of 10 °C  $\text{min}^{-1}$ , and then stabilized at 450 °C for 2 h. Upon naturally cooling down to room temperature, the resulting black  $\text{Mn}_2\text{O}_3$  products were harvested.

### 2.4 Synthesis of 3DGN/Mn-BTC

The acid-treated 3DGN was placed in a glass bottle. 1 mL of solution I mentioned above was added, followed by the adding of solution II (1 mL) after 24 h. The bottle was shaken gently for 30 seconds and placed without shaking for 24 h. The resulting 3DGN/Mn-BTC composite was washed with equal amount of ethanol/water several times, and dried in an oven at 60 °C. The color of 3DGN changed to a little white, indicating the growth of Mn-BTC crystals on the framework of 3DGN.

### 2.5 Synthesis of 3DGN/ $\text{Mn}_2\text{O}_3$

The 3DGN/Mn-BTC composite was prepared through the calcination of 3DGN/Mn-BTC precursors in a furnace under a flow of air. The temperature was raised to 450 °C at a ramping rate of 10 °C  $\text{min}^{-1}$ , and then stabilized at 450 °C for 2 h. Upon naturally cooling down to room temperature, the resulting 3DGN/ $\text{Mn}_2\text{O}_3$  products were obtained. The color of bulk material was seen to change from a little white to black, confirming the formation of  $\text{Mn}_2\text{O}_3$  on the 3DGN network. The 3DGN content in the hybrid is about 57.3%, based on the result of TG test (Fig. S2). Moreover, the weights of 3DGN (1  $\text{cm}^2$ ) and 3DGN/ $\text{Mn}_2\text{O}_3$  (1  $\text{cm}^2$ ) are approximately 0.25 and 0.45 mg, respectively. So, the proportion of 3DGN in the hybrid is about 55.6 wt.%, which is close to the TG result. Also, the loading mass of active material  $\text{Mn}_2\text{O}_3$  in the composite electrode material is 0.20  $\text{mg cm}^{-2}$ .

### 2.6 Characterization

Powder X-ray diffraction (XRD) patterns were performed on a Shimadzu XRD-6000 diffractometer using  $\text{Cu-K}\alpha$  radiation (0.15406 nm). Raman spectra were recorded using a Horiba HR800 Raman spectroscopy with excitation at 514 nm laser. The surface electronic states were investigated by X-ray photoelectron spectroscopy (XPS, Thermo-VG Scientific ESCALAB 250 using  $\text{Al-K}\alpha$  radiation) with a base pressure of  $2 \times 10^{-9}$  mbar. The field-emission scanning electron microscopy (FE-SEM) and field-emission transmission electron microscopy (FE-TEM) were performed on the ZEISS Merlin Compact and JEOL JEM-2100F, respectively. The elemental mapping analysis was carried out on an energy-dispersive X-ray spectrometry (EDS, Oxford X-Max).

## 2.7 Electrochemical measurements

All electrochemical measurements were performed on an Autolab PGSTAT302N potentiostat (Eco-Chemie) and tested in a standard three-electrode configuration equipped with a platinum plate and saturated calomel electrode (SCE) as the counter and reference electrodes, respectively. The as-prepared 3DGN, 3DGN/Mn-BTC and 3DGN/Mn<sub>2</sub>O<sub>3</sub> samples were used directly as the working electrodes without using any conductive material or binder. As a comparison, the working electrodes of pure Mn-BTC and Mn<sub>2</sub>O<sub>3</sub> were fabricated by mixing active materials with polyvinylidene fluoride (PVDF) binder and super-p at a weight ratio of 8:1:1. The as-made slurry was coated onto the graphite paper of about 1 cm<sup>2</sup> and dried at 60 °C overnight. In this work, 0.5 M Na<sub>2</sub>SO<sub>4</sub> aqueous solution was utilized as the electrolyte and all measurements were performed at 298 K. The electrochemical performances of electrodes were characterized by cyclic voltammetry (CV) and galvanostatic charge-discharge (GCD) tests within a potential range from 0 to 0.8 V versus SCE at different scan rates and current densities. The electrochemical impedance spectroscopy (EIS) measurements were carried out in the frequency range from 0.01 Hz to 100 kHz at open circuit potential with an AC perturbation of 10 mV.

## 3. Results and discussion

Fig. 1 shows the powder XRD patterns of all samples. The significant diffraction peak for 3DGN at around 26.5° corresponds to the (0 0 2) plane of graphitic carbon (JCPDS No. 75-1621). The diffraction patterns of as-prepared Mn-BTC are consistent with the previous work (Fig. S3a),<sup>61</sup> indicating the successful preparation of the same MOF formulated as Mn<sub>3</sub>(BTC)<sub>2</sub>(H<sub>2</sub>O)<sub>6</sub>. For the 3DGN/Mn-BTC composite, the characteristic peaks ascribed to 3DGN and Mn-BTC were obviously observed, which confirmed the combination of both components after the solution immersion process. The diffraction peaks of Mn-BTC are considerably broadened, indicating the anchored MOF particles are very small in size, as described in the morphology analysis below. All of diffraction peaks of manganese oxide obtained from annealing Mn-BTC precursors in air can be reasonably assigned to (211), (222), (400), (332), (431), (440) and (622) planes of the monoclinic structured Mn<sub>2</sub>O<sub>3</sub> with a space group of C2/m (JCPDS No. 41-1442) (Fig. S3b). The absence of diffraction peaks of other phases indicates the high purity of our sample and the complete phase transformation from Mn-BTC to Mn<sub>2</sub>O<sub>3</sub> through a high-temperature treatment. All diffraction peaks for the 3DGN/Mn<sub>2</sub>O<sub>3</sub> composite can be well indexed to Mn<sub>2</sub>O<sub>3</sub> apart from the characteristic peak at 2θ = 26.5° from the 3DGN substrate, which demonstrates that the crystalline Mn<sub>2</sub>O<sub>3</sub> particles has been integrated into the 3DGN substrate after annealing 3DGN/MOF precursors. The broad diffraction peaks assigned to Mn<sub>2</sub>O<sub>3</sub> also confirmed the small particle size.

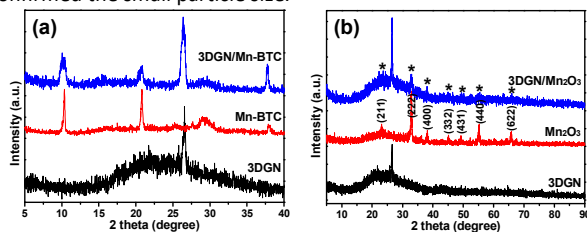


Fig. 1 Powder XRD patterns of (a) 3DGN, Mn-BTC, 3DGN/Mn-BTC, and (b) 3DGN, Mn<sub>2</sub>O<sub>3</sub>, 3DGN/Mn<sub>2</sub>O<sub>3</sub>.

The chemical composition and oxidation state of the 3DGN/Mn<sub>2</sub>O<sub>3</sub> composite were identified from XPS measurements. The survey XPS spectra (Fig. 2a) suggested the presence of C, Mn and O. The peak at 284.8 eV in the XPS spectrum (Fig. 2b) of C 1s is originated from the sp<sup>2</sup>-hybridized carbon atoms from 3DGN.<sup>62</sup> Two peaks at 641.6 and 653.3 eV in the XPS spectrum (Fig. 2c) of Mn 2p can be assigned to the Mn 2p<sub>3/2</sub> and Mn 2p<sub>1/2</sub> spin-orbit states, respectively. The spin energy separation between both peaks is 11.7 eV, matching with that of the standard Mn<sub>2</sub>O<sub>3</sub>.<sup>63</sup> As shown in Fig. 2d, the peak at 531.8 eV is assigned to O-C (O 1s) of the graphene sheet<sup>64</sup> and the peak at 530.0 eV can be ascribed to O-Mn (O 1s) of Mn<sub>2</sub>O<sub>3</sub>.<sup>65-67</sup> This result indicates the formation of Mn<sub>2</sub>O<sub>3</sub> particles anchored-3DGN after annealing 3DGN/Mn-BTC in air.

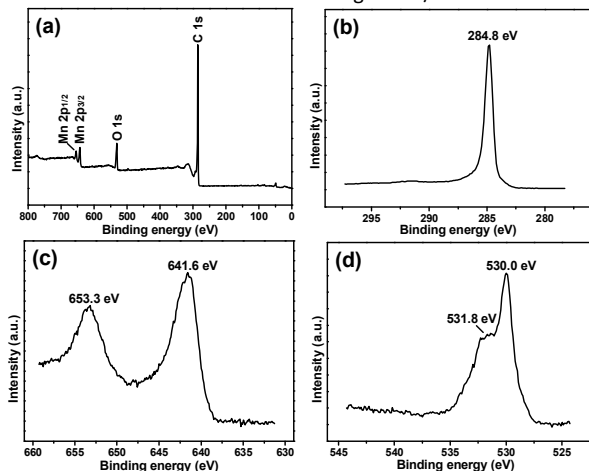
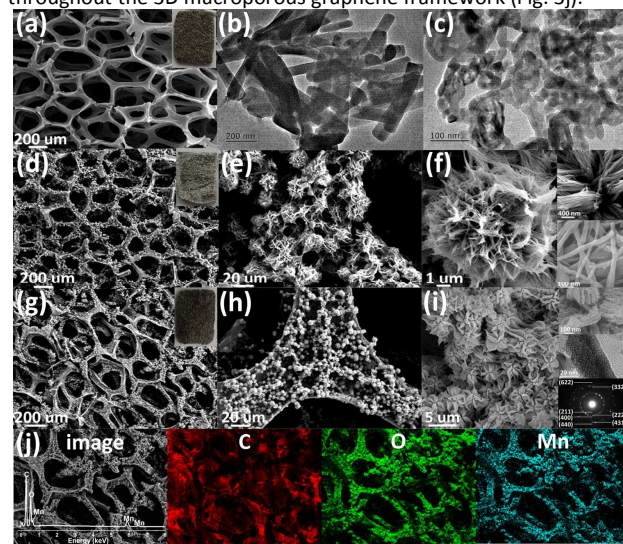


Fig. 2 XPS spectra of the 3DGN/Mn<sub>2</sub>O<sub>3</sub> composite: (a) Survey spectrum, (b) C 1s spectrum, (c) Mn 2p spectrum, and (d) O 1s spectrum.

Field-emission scanning electron microscopy (FESEM) and transmission electron microscopy (FETEM) images of as-synthesized samples are illustrated in Fig. 3. 3DGN exhibited a free-standing, monolithic and uniform porous structure (Fig. 3a). The pristine Mn-BTC displayed a well-defined long-nanorod morphology with an average diameter of about 80 nm and a length of more than half a micrometer (Fig. 3b), as observed in the literature.<sup>60</sup> After the calcination of Mn-BTC in air, the resulting Mn<sub>2</sub>O<sub>3</sub> particles inherited a short-nanorod shape, and the average size (~20 nm in diameter and ~60 nm in length) was significantly shrunken compared with MOF precursors due to the loss of hydrogen and carbon atoms upon heating (Fig. 3c), evidenced in other MOF-derived metal oxides.<sup>68,69</sup> The whole framework of 3DGN remained intact without spalling after the growth of Mn-BTC crystals except the color change of 3DGN, and the surface of 3DGN became rough compared to the original surface (Fig. 3d). As shown in Fig. 3e and Fig. 3f, uniform flower-like Mn-BTC microspheres with the diameter of ~20 μm were grown densely on the surface of 3DGN, and in fact these flower-shaped spheres comprise of numerous nanowires with a smooth surface. High-magnification SEM images further confirmed that these Mn-BTC nanowires have an average diameter of approximately ~50 nm and a length from several-hundred nanometers to several micrometers (Fig. 3f inset). Notably, the Mn-BTC nanowires coated on 3DGN and pure Mn-BTC crystals show slightly different morphologies, indicating that the unique feature of 3DGN has an influence on the assembly reaction of MOF precursors (Mn(II) ions, H<sub>3</sub>BTC ligands). The obtained 3DGN/Mn<sub>2</sub>O<sub>3</sub>

bulk material still kept the completeness after annealing 3DGN/Mn-BTC in air (Fig. 3g), and the color of the sample turned back to black due to the high-temperature oxidation of MOF. The obtained  $\text{Mn}_2\text{O}_3$  particles exhibited a nanowire stacking flower-like morphology with the diameter of several micrometers (Fig. 3h, Fig. 3i). It can be seen that these flowers are irregular and exhibit a significantly decrease in size relative to Mn-BTC flower-like microspheres in the 3DGN/Mn-BTC sample. However, these  $\text{Mn}_2\text{O}_3$  particles still maintained the nanowire shape of MOF precursors, and the diameter size of nanowires is in the range of 30~40 nm. The decrease in size for  $\text{Mn}_2\text{O}_3$  compared with Mn-BTC in 3DGN/Mn-BTC can be mainly ascribed to the release of organic parts during the calcination. Notably, the observed  $\text{Mn}_2\text{O}_3$  nanowires are discontinuous and interconnected, and the surface of nanowires is much rougher than that of Mn-BTC because of the release of gaseous molecules after the calcination of MOF. This result further demonstrates that MOFs can be converted to the designed metal oxides with controlled morphologies and sizes through the high-temperature treatment.<sup>70,71</sup> In our case, organic linkers in MOF can efficiently prevent the aggregation of the resulting nanometer particles in the primary nanowire-shaped MOF, generating numerous voids in the final microflowers and nanowires with coarse surface. These voids will make the maximum proportion of the surfaces accessible to the electrolyte leading to high capacitance. The selected-area electron diffraction (SAED) pattern of  $\text{Mn}_2\text{O}_3$  nanowires in the composite showed a set of well-defined concentric rings, indicating their polycrystalline structure. The corresponding crystal planes are consistent with the XRD analysis. Moreover, the complete coverage of  $\text{Mn}_2\text{O}_3$  layers can be also evidenced by energy-dispersive X-ray spectroscopy (EDS). The elemental mapping images of carbon, oxygen and manganese clearly verified the homogeneous coating of  $\text{Mn}_2\text{O}_3$  particles throughout the 3D macroporous graphene framework (Fig. 3j).



**Fig. 3** (a) SEM image of 3DGN (Inset: the photograph of 3DGN); TEM images of (b) Mn-BTC and (c)  $\text{Mn}_2\text{O}_3$ ; SEM images of 3DGN/Mn-BTC at (d, e) low magnifications (Inset: the photograph of 3DGN/Mn-BTC) and (f) high magnifications (Inset: SEM images of nanowires); SEM images of 3DGN/ $\text{Mn}_2\text{O}_3$  at (g, h) low magnifications (Inset: the photograph of 3DGN/ $\text{Mn}_2\text{O}_3$ ) and (i) high magnifications (Inset: SEM image of nanowires (top), TEM image of a single nanowire (middle), and the corresponding SAED

pattern (bottom)); (j) The elemental mapping distribution of 3DGN/ $\text{Mn}_2\text{O}_3$  (Inset: EDS spectrum).

The free-standing 3DGN, 3DGN/Mn-BTC and 3DGN/ $\text{Mn}_2\text{O}_3$  materials were used directly as working electrodes. Electrochemical performances of all samples were investigated by cyclic voltammetry (CV) and galvanostatic charge/discharge (GCD) measurements in three-electrode beaker cell in a 0.5 M  $\text{Na}_2\text{SO}_4$  electrolyte (Fig. 4). In the comparison experiments, the pure Mn-BTC and  $\text{Mn}_2\text{O}_3$  powders were also used as the working electrodes according to the conventional electrode preparation method described in the experimental section.

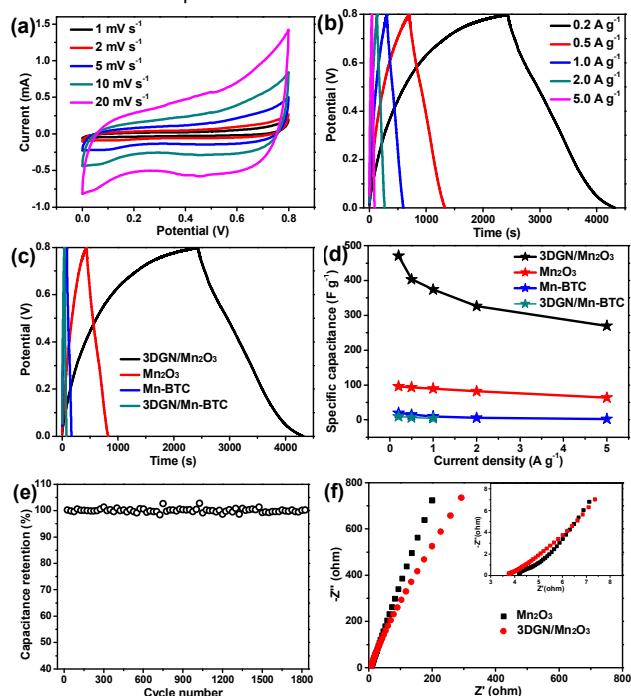


**Fig. 4.** (a) CV curves of the 3DGN/ $\text{Mn}_2\text{O}_3$  composite electrode at different scan rates; (b) GCD curves of 3DGN/ $\text{Mn}_2\text{O}_3$  at different current densities; (c) GCD curves of the electrodes of Mn-BTC,  $\text{Mn}_2\text{O}_3$ , 3DGN/Mn-BTC and 3DGN/ $\text{Mn}_2\text{O}_3$  at  $0.2 \text{ A g}^{-1}$ ; (d) Specific capacitance as a function of the current density of the electrodes of Mn-BTC,  $\text{Mn}_2\text{O}_3$ , 3DGN/Mn-BTC and 3DGN/ $\text{Mn}_2\text{O}_3$ ; (e) Cycling performance of 3DGN/ $\text{Mn}_2\text{O}_3$  during 1800 charge-discharge cycles at  $1 \text{ A g}^{-1}$ ; (f) Nyquist plots of  $\text{Mn}_2\text{O}_3$  and 3DGN/ $\text{Mn}_2\text{O}_3$  (Inset: the magnification of the high frequency).

The CV curves of the 3DGN/ $\text{Mn}_2\text{O}_3$  electrode at different scan rates are shown in Fig. 4a. The curves presented an approximately rectangular and symmetric shape, indicating the pseudocapacitive nature with fast charge/discharge processes. CV curves basically kept the same shape and still remained approximately rectangular upon increasing the scan rates from 1 to  $20 \text{ mV s}^{-1}$ , demonstrating the remarkable electrochemical reversibility. This can be attributed to the hierarchically interconnected and porous nanostructure, and electrically conductive feature of 3DGN, which allow great access of electrolyte to the active surface of electrode materials. CV curves with similar behaviors have been also observed in the 3DGN/Mn-BTC, Mn-BTC,  $\text{Mn}_2\text{O}_3$ , and 3DGN electrodes (Figs. S4-S7). The GCD curves of Mn-BTC,  $\text{Mn}_2\text{O}_3$ , 3DGN, 3DGN/Mn-BTC, and 3DGN/ $\text{Mn}_2\text{O}_3$  electrodes measured between 0 and 0.8 V at different current densities are shown in Figs. S4-S7 and Fig. 4b. The areas of GCD curves decreased with increasing the current densities from 0.2 to 5

$\text{A g}^{-1}$ . It should be noted that the GCD curves of 3DGN/ $\text{Mn}_2\text{O}_3$  are not strictly symmetrical especially for the case at low current density, indicating the absence of complete reversibility for the redox. The GCD curves at  $0.2 \text{ A g}^{-1}$  of the 3DGN and 3DGN/ $\text{Mn}_2\text{O}_3$  electrodes are shown in Fig. S8. It can be seen that the voltage of 3DGN approximately varies linearly with time, and the curve is close to isosceles triangle, which revealed the ideal double-layer capacitive behavior. Different from 3DGN, the charge/discharge curve of 3DGN/ $\text{Mn}_2\text{O}_3$  exhibits a slight bend and a longer charge/discharge time. This phenomenon is mainly ascribed to the pseudo-capacitance of  $\text{Mn}_2\text{O}_3$ . Thus, the specific capacitance of the 3DGN/ $\text{Mn}_2\text{O}_3$  composite electrode is composed of both the double-layer capacitance of 3DGN and Faradaic redox pseudo-capacitance of  $\text{Mn}_2\text{O}_3$ . Fig. 4c shows the charge-discharge curves of the 3DGN/ $\text{Mn}_2\text{O}_3$ , 3DGN/Mn-BTC, Mn-BTC and  $\text{Mn}_2\text{O}_3$  electrodes at a current density of  $0.2 \text{ A g}^{-1}$ . The specific capacitance of the electrodes at different current densities can be calculated from these curves according to the following equation:  $C = It/\Delta Vm$ , where  $C$  ( $\text{F g}^{-1}$ ) is the specific capacitance,  $I$  is the discharge current,  $t$  is the total discharge time,  $\Delta V$  is the potential drop during discharge, and  $m$  is the mass of active materials in a single electrode. It is noted that the specific capacitance of 3DGN/ $\text{Mn}_2\text{O}_3$  was measured to be  $471.1 \text{ F g}^{-1}$  ( $0.21 \text{ F cm}^{-2}$ ) at  $0.2 \text{ A g}^{-1}$ , much higher than those for as-prepared  $\text{Mn}_2\text{O}_3$  ( $96.3 \text{ F g}^{-1}$ ), Mn-BTC ( $20.4 \text{ F g}^{-1}$ ), 3DGN ( $13.75 \text{ F g}^{-1}$ ,  $0.0034 \text{ F cm}^{-2}$ ) and 3DGN/Mn-BTC ( $9.6 \text{ F g}^{-1}$ ). The specific capacitance observed in 3DGN/ $\text{Mn}_2\text{O}_3$  exhibits nearly 5- and 35-fold enhancements relative to pure  $\text{Mn}_2\text{O}_3$  and 3DGN, respectively, indicating that the hierarchically interconnected and porous structures of 3DGN/ $\text{Mn}_2\text{O}_3$  and excellent electrically conductive ability of 3DGN could offer more electrochemically active sites to take part in the process of energy storage and then improve the capacitive performance of electrodes. It was found that the specific capacitance of 3DGN can be negligible due to their much lower value compared to that for 3DGN/ $\text{Mn}_2\text{O}_3$ . In fact, the specific capacitance of 3DGN/ $\text{Mn}_2\text{O}_3$  is considerably higher than those found in the  $\text{Mn}_2\text{O}_3$  electrode materials with various morphologies (such as nanocubics, films, microspheres and micropolyhedrons).<sup>72-74</sup>

To probe the rate capability of the electrodes, the specific capacitances of 3DGN/ $\text{Mn}_2\text{O}_3$  electrode have been examined at different current densities. Fig. 4d shows the summary plots of the specific capacitances vs. the current densities. The specific capacitance of 3DGN/ $\text{Mn}_2\text{O}_3$  is 471.1, 403.1, 374.2, 326.5, and  $270.0 \text{ F g}^{-1}$  at 0.2, 0.5, 1, 2, and  $5 \text{ A g}^{-1}$ , respectively. The 3DGN/ $\text{Mn}_2\text{O}_3$  electrode preserved 57.3% of its initial capacitance value at  $0.2 \text{ A g}^{-1}$  upon increasing the current density to  $5 \text{ A g}^{-1}$ . The capacitance decreased upon raising discharge current densities, which can be ascribed to the resistance increase in  $\text{Mn}_2\text{O}_3$  and the relatively insufficient faradic redox reaction at higher current densities. This remarkable rate capabilities observed in our composite can be attributed to the hierarchically interconnected and porous structure of the materials, which allows the facile penetration of electrolytes to promote the redox reactions. It also guarantees that relatively highly electrolyte-accessible areas and the porous features are greatly beneficial for the transport and diffusion of electrolyte ions during the rapid charge-discharge

process. For this type of composite electrode, the free-standing macroporous 3DGN becomes the sustentation of  $\text{Na}^+$  ions and promotes the Faradaic reactions of the active materials at high current densities for energy storage. As we all know, the good long-term cycle stability of electrode materials is an important criterion for supercapacitors. The specific capacitance of the 3DGN/ $\text{Mn}_2\text{O}_3$  electrode as a function of cycle numbers at a current density of  $1 \text{ A g}^{-1}$  for up to 1800 charge-discharge cycles was illustrated in Fig. 4e. The specific capacitances of the 3DGN/ $\text{Mn}_2\text{O}_3$  electrode remained unchanged during the whole cycling tests. As the substrate of active material  $\text{Mn}_2\text{O}_3$ , the macroporous 3DGN not only offers an extremely highly electrolyte-accessible area and keeps the active materials from falling off into the electrolyte, but also serves as a structural buffer for the large volume expansion-contraction during the redox reaction process. As a result, the 3DGN/ $\text{Mn}_2\text{O}_3$  electrode exhibited an excellent electrochemical stability. Fig. 4f shows the Nyquist plots of the  $\text{Mn}_2\text{O}_3$  and 3DGN/ $\text{Mn}_2\text{O}_3$  electrodes. As can be seen in the magnification Nyquist plots (inset), the bulk solution resistance of 3DGN/ $\text{Mn}_2\text{O}_3$  ( $3.79 \Omega$ ) is smaller than  $\text{Mn}_2\text{O}_3$  ( $4.20 \Omega$ ), which can be attributed to the improved electrical conductivity caused by the introduction of 3DGN. At a high frequency region, the semicircular loops of  $\text{Mn}_2\text{O}_3$  and 3DGN/ $\text{Mn}_2\text{O}_3$  are very small, and the diameter for 3DGN/ $\text{Mn}_2\text{O}_3$  is smaller than that for  $\text{Mn}_2\text{O}_3$ , implying that the 3DGN/ $\text{Mn}_2\text{O}_3$  composite electrode provides a better pathway for ion transfer and electron transport. In the mid-frequency region, a straight line inclined at a high angle with the real axis was observed, representing a Warburg element of the diffusion limitation. At low frequency region, both materials exhibited a straight oblique line, indicating the typical capacitive behavior of supercapacitor electrodes.

It should be mentioned here that the 3DGN/ $\text{Mn}_2\text{O}_3$  composite keeps obvious advantages compared with the reported pure  $\text{Mn}_2\text{O}_3$ <sup>72-74</sup> and  $\text{Mn}_2\text{O}_3$ -carbon hybrids<sup>75,76</sup> in the aspects of specific capacitance and cycling stability, even comparable to the free-standing  $\text{MnO}_2$ /3DGN materials (Table 1).<sup>77-82</sup> The remarkable electrochemical performance for 3DGN/ $\text{Mn}_2\text{O}_3$  can be attributed to the synergetic effect of  $\text{Mn}_2\text{O}_3$  and 3DGNs components. Firstly, the active material  $\text{Mn}_2\text{O}_3$  with a nanowire morphology can provide a high faradic capacitance for supercapacitors, while the hierarchically porous structure of 3DGNs/ $\text{Mn}_2\text{O}_3$  facilitates the fast transport of electrons and ions among active materials. Secondly, the interconnected and highly electronic conductivity of 3DGN provides efficient tunnels and more available active sites for the diffusion of electrolyte ions and electrons transport. Finally, 3DGN can act as a structural buffer for the large volume expansion during the redox reaction, and has an intensely electrical contact with active materials  $\text{Mn}_2\text{O}_3$  upon cycling, resulting in a high rate capability as well as excellent cycling stability.

**Table 1** Summary of capacitive performances of reported Mn<sub>2</sub>O<sub>3</sub>, Mn<sub>2</sub>O<sub>3</sub>-carbon and MnO<sub>2</sub>/3DGN electrode materials for supercapacitors.

Electrode material	Specific capacitance (based on the active material)	Cycling stability	Refs
Mn <sub>2</sub> O <sub>3</sub> nanowires/3DGN	471.1 F g <sup>-1</sup> (0.2 A g <sup>-1</sup> )	1800 cycles (~100%)	this work
Mn <sub>2</sub> O <sub>3</sub> films	<189.9 F g <sup>-1</sup> (25 mV s <sup>-1</sup> )	300 cycles (<78.6%)	72
Mn <sub>2</sub> O <sub>3</sub> spheres or polyhedrons	<202 F g <sup>-1</sup>	400 cycles (<100%)	73
Mn <sub>2</sub> O <sub>3</sub> nanocubics	191.1 F g <sup>-1</sup> (0.1 A g <sup>-1</sup> )	3000 cycles (108%)	74
Mn <sub>2</sub> O <sub>3</sub> /2DGN	300 F g <sup>-1</sup> (0.05 A g <sup>-1</sup> )	1000 cycles (>90%)	75
Mn <sub>2</sub> O <sub>3</sub> /carbon aerogel microbead	368.01 F g <sup>-1</sup> (1 mV s <sup>-1</sup> )	5000 cycles (90%)	76
MnO <sub>2</sub> nanospheres/3DGN	709.8 F g <sup>-1</sup> (0.2 A g <sup>-1</sup> )	1000 cycles (97.6%)	77
MnO <sub>2</sub> nanoparticles/3DGN	242 F g <sup>-1</sup> (1 A g <sup>-1</sup> )	1000 cycles (89.6%)	78
MnO <sub>2</sub> nanoflakes/3DGN	210 F g <sup>-1</sup> (2 A g <sup>-1</sup> )	4000 cycles	79
MnO <sub>2</sub> nanofibers/3DGN	670 F g <sup>-1</sup> (10 mV s <sup>-1</sup> )	---	80
MnO <sub>2</sub> nanosheets/3DGN	465 F g <sup>-1</sup> (2 mV s <sup>-1</sup> )	---	81
MnO <sub>2</sub> (various shapes)/3DGN	560 F g <sup>-1</sup> (0.2 A g <sup>-1</sup> )	1000 cycles (79%)	82

## Conclusions

In summary, a simple and cost-effective protocol to fabricate Mn<sub>2</sub>O<sub>3</sub> nanowires-coated on 3DGN via a two-step process has been developed in this work. This novel free-standing 3DGN/Mn<sub>2</sub>O<sub>3</sub> hybrid can be directly employed as an electrode for supercapacitors and has demonstrated remarkable electrochemical performances including a high specific capacitance, superior rate capability and excellent long-term cycling stability. The excellent electrochemical properties can be reasonably attributed to the synergistic integration of highly electrical conductivity and large surface area of 3DGN as well as the superior pseudocapacitive activity of Mn<sub>2</sub>O<sub>3</sub> nanowires. Our work opens up an avenue to rationally design and construct hierarchically porous and free-standing 3DGN/MOF-derived metal oxides electrode materials with outstanding electrochemical properties for their applications in the next-generation energy conversion/storage devices.

## Acknowledgements

This work was supported by National Natural Science Foundation (51102119, 51272095), Natural Science Foundation of Jiangsu Province (BK20151328), Qing Lan Project of Jiangsu Province, the project of the Priority Academic Program Development of Jiangsu Higher Education Institutions, China Postdoctoral Science Foundation (2014M561578) and Jiangsu Planned Projects for Postdoctoral Research Funds (1401109C).

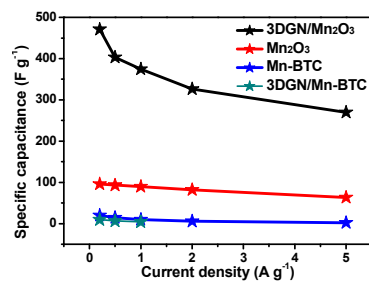
## References

- X. F. Wang, X. H. Lu, B. Liu, D. Chen, Y. X. Tong and G. Z. Shen, *Adv. Mater.*, 2014, **26**, 4763-4782.
- P. Simon, Y. Gogotsi and B. Dunn, *Science*, 2014, **343**, 1210-1211.
- X. H. Lu, M. H. Yu, G. M. Wang, Y. X. Tong and Y. Li, *Energy Environ. Sci.*, 2014, **7**, 2160-2181.
- Y. G. Wang and Y. Y. Xia, *Adv. Mater.*, 2013, **25**, 5336-5342.
- J. R. Miller and P. Simon, *Science*, 2008, **321**, 651-652.
- V. Augustyn, P. Simon and B. Dunn, *Energy Environ. Sci.*, 2014, **7**, 1597-1614.
- W. Y. Li, K. B. Xu, L. An, F. R. Jiang, X. Y. Zhou, J. M. Yang, Z. G. Chen, R. J. Zou, J. Q. Hu, *J. Mater. Chem.*, 2014, **2**, 1443-1447.
- G. P. Wang, L. Zhang and J. J. Zhang, *Chem. Soc. Rev.*, 2012, **41**, 797-828.
- W. Y. Li, Q. Liu, Y. G. Sun, J. Q. Sun, R. J. Zou, G. Li, X. H. Hu, G. S. Song, G. X. Ma, J. M. Yang, Z. G. Chen, J. Q. Hu, *J. Mater. Chem.*, 2012, **22**, 14864-14867.

- H. Furukawa, K. E. Cordova and M. O'Keeffe, *Science*, 2013, **341**, 1230444.
- Y. Zhang, J. Wang, X. F. Yan, X. Q. Liu, H. Zhou and A. H. Yuan, *Micropor. Mesopor. Mat.*, 2014, **184**, 15-20.
- A. H. Yuan, H. Zhou, G. W. Diao, P. D. Southon, C. J. Kepert and L. Liu, *Int. J. Hydrogen Energ.*, 2014, **39**, 884-889.
- M. O'Keeffe and O. M. Yaghi, *Chem. Rev.*, 2012, **112**, 675-702.
- F. A. A. Paz, J. Klinowski, S. M. F. Vilela, J. P. C. Tomé, J. A. S. Cavaleiro and J. Rocha, *Chem. Soc. Rev.*, 2012, **41**, 1088-1110.
- J. Wang, Y. Zhang, X. Q. Liu, J. Xiao, H. Zhou and A. H. Yuan, *Micropor. Mesopor. Mat.*, 2012, **159**, 100-104.
- D. J. Tranchemontagne and J. L. Mendoza-Cortés, *Chem. Soc. Rev.*, 2009, **38**, 1257-1283.
- L. Yu, B. Y. Xia, X. Wang, X. W. Lou, *Adv. Mater.*, 2016, **28**, 92-97.
- B. Y. Xia, Y. Yan, N. Li, H. B. Wu, X. W. Lou, X. Wang, *Nat. Energy*, 2016, **1**, 15006.
- H. B. Wu, B. Y. Xia, L. Yu, X. Y. Yu, X. W. Lou, *Nat. Commun.*, 2015, **6**, 6512.
- H. Hu, B. Y. Guan, B. Y. Xia, X. W. Lou, *J. Am. Chem. Soc.*, 2015, **137**, 5590-5595.
- L. Lux, K. Williams and S. Q. Ma, *CrystEngComm*, 2015, **17**, 10-22.
- Y. H. Song, X. Li, C. T. Wei, J. Y. Fu, F. G. Xu, H. J. Tan, J. Tang and L. Wang, *Sci. Rep.*, 2015, **5**, 8401.
- T. Y. Ma, S. Dai, M. Jaroniec, S. Z. Qiao, *J. Am. Chem. Soc.*, 2014, **136**, 13925-13931.
- W. J. Meng, W. Chen, L. Zhao, Y. Huang, M. S. Zhu, Y. Huang, Y. Q. Fu, F. X. Geng, J. Yu, X. F. Chen and C. Y. Zhi, *Nano Energy*, 2014, **8**, 133-140.
- B. Yan, L. Chen, Y. J. Liu, G. X. Zhu, C. G. Wang, H. Zhang, G. Yang, H. T. Ye and A. H. Yuan, *CrystEngComm*, 2014, **16**, 10227-10234.
- L. Zhang, H. B. Wu and X. W. Lou, *J. Am. Chem. Soc.*, 2013, **135**, 10064-10672.
- A. Banerjee, U. Singh, V. Aravindan, M. Srinivasan and S. Ogale, *Nano Energy*, 2013, **2**, 1158-1163.
- T. K. Kim, K. J. Lee, J. Y. Cheon, J. H. Lee, S. H. Joo and H. R. Moon, *J. Am. Chem. Soc.*, 2013, **135**, 8940-8946.
- X. D. Xu, R. G. Cao, S. Jeong and J. Cho, *Nano Lett.*, 2012, **12**, 4988-4991.
- A. Banerjee, V. Aravindan, S. Bhatnagar, D. Mhamane, S. Madhavi and S. Ogale, *Nano Energy*, 2013, **2**, 890-896.
- L. Zhang, H. B. Wu, S. Madhavi, H. H. Hng and X. W. Lou, *J. Am. Chem. Soc.*, 2012, **134**, 17388-17391.
- J. U. Park, H. J. Lee, W. Cho, C. Jo and M. Oh, *Adv. Mater.*, 2011, **23**, 3161-3164.
- D. Li, Y. R. Liu, B. P. Lin, Y. Sun, H. Yang and X. Q. Zhang, *Prog. Chem.*, 2015, **27**, 404-415.
- K. Mondal, C. Y. Tsai, S. Stout and S. Talapatra, *Mater. Lett.*, 2015, **148**, 142-146.
- X. H. Cao, B. Zheng, W. H. Shi, J. Yang, Z. X. Fan, Z. M. Luo, X. H. Rui, B. Chen, Q. Y. Yan and H. Zhang, *Adv. Mater.*, 2015, **27**, 4695-4701.
- Z. Y. Ji, X. P. Shen, H. Zhou and K. M. Chen, *Ceram. Int.*, 2015, **41**, 8710-8716.

- 37 Z. Y. Ji, J. L. Zhao, X. Y. Yue, A. H. Yuan, H. Zhou and J. Yang, *Ceram. Int.*, 2015, **41**, 13509-13515.
- 38 L. B. Ma, X. P. Shen, Z. Y. Ji, G. X. Zhu and H. Zhou, *Chem. Eng. J.*, 2014, **252**, 95-103.
- 39 Z. Y. Ji, X. P. Shen, M. Z. Li, H. Zhou, G. X. Zhu and K. M. Chen, *Nanotechnology*, 2013, **24**, 115603 (9pp).
- 40 H. Jiang, J. Ma and C. Z. Li, *Adv. Mater.*, 2012, **24**, 4197-4202.
- 41 L. Y. Yuan, X. H. Lu, X. Xia, T. Zhai, J. J. Dai, F. C. Zhang, B. Hu, X. Wang, L. Gong, J. Chen, C. G. Hu, Y. X. Tong, J. Zhou and Z. L. Wang, *ACS Nano*, 2011, **6**, 656-661.
- 42 Z. Y. Ji, J. L. Wu, X. P. Shen, H. Zhou and H. T. Xi, *J. Mater. Sci.*, 2011, **46**, 1190-1195.
- 43 X. P. Shen, J. L. Wu, S. Bai and H. Zhou, *J. Alloy. Compd.*, 2010, **506**, 136-140.
- 44 R. R. Bi, X. L. Wu, F. F. Cao, L. Y. Jiang, Y. G. Guo and L. J. Wan, *J. Phys. Chem. C*, 2010, **114**, 2448-2451.
- 45 S. J. He and W. Chen, *Nanoscale*, 2015, **7**, 6957-6990.
- 46 S. Mao, G. H. Lu and J. H. Chen, *Nanoscale*, 2015, **7**, 6924-6943.
- 47 X. H. Xia, D. L. Chao, Y. Q. Zhang, Z. X. Shen and H. J. Fan, *Nano Today*, 2014, **9**, 785-807.
- 48 U. Patil, S. C. Lee, S. Kulkarni, J. S. Sohn, M. S. Nam, S. Han and S. C. Jun, *Nanoscale*, 2015, **7**, 6999-7021.
- 49 X. H. Cao, Z. Y. Yin and H. Zhang, *Energy. Environ. Sci.*, 2014, **7**, 1850-1865.
- 50 X. H. Cao, B. Zhang, X. H. Rui, W. H. Shi, Q. Y. Yan and H. Zhang, *Angew. Chem. Int. Ed.*, 2014, **53**, 1404-1409.
- 51 H. Zhou, J. Zhang, D. Ji, A. H. Yuan and X. P. Shen, *Micropor. Mesopor. Mat.*, DOI: 10.1016/j.micromeso.2016.04.007.
- 52 J. Zhang, D. Ji, H. Zhou, X. F. Yan and A. H. Yuan, *J. Nanosci. Nanotech.*, DOI: 10.1166/jnn.2016.12685.
- 53 H. Zhou, J. Zhang, J. Zhang, X. F. Yan, X. P. Shen and A. H. Yuan, *Int. J. Hydrogen Energ.*, 2015, **40**, 12275-12285.
- 54 H. Zhou, X. Q. Liu, J. Zhang, X. F. Yan, Y. J. Liu and A. H. Yuan, *Int. J. Hydrogen Energ.*, 2014, **39**, 2160-2167.
- 55 J. Zhang, X. Q. Liu, H. Zhou, X. F. Yan, Y. J. Liu and A. H. Yuan, *RSC Adv.*, 2014, **4**, 28908-28913.
- 56 Z. P. Chen, W. C. Ren, L. B. Gao, B. L. Liu, S. F. Pei and H. M. Cheng, *Nat. Mater.*, 2011, **10**, 424-428.
- 57 Z. H. Ni, T. Yu, Y. H. Lu, Y. Y. Wang, Y. P. Feng and Z. X. Shen, *ACS Nano*, 2008, **2**, 2301-2305.
- 58 D. Graf, F. Molitor, K. Ensslin, C. Stampfer, A. Jungen, C. Hierold and L. Wirtz, *Nano Lett.*, 2007, **7**, 238-242.
- 59 A. C. Ferrari, *Solid State Commun.*, 2007, **143**, 47-57.
- 60 K. M. L. Taylor, W. J. Rieter and W. B. Lin, *J. Am. Chem. Soc.*, 2008, **130**, 14358-14359.
- 61 F. C. Zheng, G. L. Xia, Y. Yang, Q. W. Chen, *Nanoscale*, 2015, **7**, 9637-9645.
- 62 G. D. Ruan, Z. Z. Sun, Z. W. Peng and J. M. Tour, *ACS Nano*, 2011, **5**, 7601-7607.
- 63 A. A. Audi and P. M. A. Sherwood, *Surf. Interface Anal.*, 2002, **33**, 274-282.
- 64 H. C. Schniepp, J. L. Li, M. J. McAllister, H. Sai, M. Herrera-Alonso, D. H. Adamson, R. K. Prud'homme, R. Car, D. A. Saville and I. A. Aksay, *J. Phys. Chem. B*, 2006, **110**, 8535-8539.
- 65 R. T. Dong, H. L. Wang, Q. Zhang, X. T. Xu, F. Wang and B. Lin, *ACS Appl. Mater. Inter.*, 2015, **7**, 9526-9533.
- 66 B. C. Sekhar and N. Kalaiselvi, *CrystEngComm*, 2015, **17**, 5038-5045.
- 67 Q. Li, L. W. Yin, Z. Q. Li, X. K. Wang, Y. X. Qi and J. Y. Ma, *ACS Appl. Mater. Inter.*, 2013, **5**, 10975-10984.
- 68 H. Guo, T. T. Li, W. W. Chen, L. X. Liu, X. Q. Yang, Y. P. Wang and Y. C. Guo, *Nanoscale*, 2014, **6**, 15168-15174.
- 69 Z. Q. Wang, X. Li, H. Xu, Y. Yang, Y. L. Cui, H. G. Pan, Z. Y. Wang, B. L. Chen and G. D. Qian, *J. Mater. Chem. A*, 2014, **2**, 12571-12575.
- 70 W. Xia, A. Mahmood, R. Q. Zou and Q. Xu, *Energy. Environ. Sci.*, 2015, **8**, 1837-1866.
- 71 L. Lux, K. Williams and S. Q. Ma, *CrystEngComm*, 2015, **17**, 10-22.
- 72 W. Y. Li, J. J. Shao, Q. Liu, X. J. Liu, X. Y. Zhou and J. Q. Hu, *Electrochim. Acta*, 2015, **157**, 108-114.
- 73 S. L. Chen, F. Liu, Q. J. Xiang, X. H. Feng and G. H. Qiu, *Electrochim. Acta*, 2013, **106**, 360-371.
- 74 C. K. Lin, K. H. Chuang, C. Y. Lin, C. Y. Tsay and C. Y. Chen, *Surf. Coat. Tech.*, 2007, **202**, 1272-1276.
- 75 K. W. Park, *J. Mater. Chem. A*, 2014, **2**, 4292-4298.
- 76 X. Y. Wang, L. Liu, X. Y. Wang, L. H. Yi, C. Y. Hu and X. Y. Zhang, *Mat. Sci. Eng. B*, 2011, **176**, 1232-1238.
- 77 B. Wei, L. D. Wang, Q. H. Miao, Y. N. Yuan, P. Dong, R. Vajtai and W. D. Fei, *Carbon*, 2015, **85**, 249-260.
- 78 S. H. Wu, W. F. Chen and L. F. Yan, *J. Mater. Chem. A*, 2014, **2**, 2765-2772.
- 79 X. X. Sun, H. J. Wang, Z. B. Lei, Z. H. Liu and L. L. Wei, *RSC Adv.*, 2014, **4**, 30233-30240.
- 80 U. M. Patil, J. S. Sohn, S. B. Kulkarni, H. G. Park, Y. M. Jung, K. V. Gurav, J. H. Kim and S. C. Jun, *Mater. Lett.*, 2014, **119**, 135-139.
- 81 Y. M. He, W. J. Chen, X. D. Li, Z. X. Zhang, J. C. Fu, C. H. Zhao and E. Q. Xie, *ACS Nano*, 2013, **7**, 174-182.
- 82 X. C. Dong, X. W. Wang, J. Wang, H. Song, X. G. Li, L. H. Wang, M. B. Chan-Park, C. M. Li and P. Chen, *Carbon*, 2012, **50**, 4865-4870.





The 3DGN and MOF-derived metal oxide composites as a free-standing electrode for supercapacitors for the first time. The designed electrode exhibits a high specific capacitance, good rate capability and excellent long-cycle stability, which can be attributed to the synergistic effect of 3DGN and metal oxide.